Tiled-Block Image Reconstruction by Wavelet-Based, Parallel Filtered Back-Projection

DOI:
10.1109/JSEN.2016.2546182

Document Version
Accepted author manuscript

Tiled-Block Image Reconstruction by Wavelet-Based, Parallel Filtered Back-Projection

Jorge Guevara Escobedo and Krikor B. Ozanyan, *Senior Member, IEEE*

***Abstract*— We demonstrate an algorithm, relevant to tomography sensor systems, to obtain images from the parallel reconstruction of essentially localized elements at different scales. This is achieved by combining methodology to reconstruct images from limited and/or truncated data, with the time-frequency capabilities of the Wavelet Transform. Multi-scale, as well as time-frequency, localization properties of the separable two-dimensional wavelet transform are exploited as an approach for faster reconstruction. The speed up is realized not only by reducing the computation load on a single processor, but also by achieving the parallel reconstruction of several tiled blocks. With tiled-block image reconstruction by wavelet-based, parallel filtered back-projection we measure more than 36 times gain in speed, compared to standard filtered back-projection.**

***Index Terms*— image reconstruction, computed tomography, data processing algorithms, parallel processing, wavelet transform.**

I. Introduction

Across many applications, it is common to identify the need of information about an object, without altering its physical structure. Fortunately, there are numerous methods allowing radiation, either emitted or transmitted, to be employed to obtain cross-sectional images characterizing the inner structure of an object. The mathematical foundation behind such an approach was developed by Johann Radon in 1917 [1] and several decades later, in 1972, experimentally implemented by Hounsfield [2] resulting in the demonstration of the first Computed Tomography (CT) scanner.

The main motivation for this work was the existing body of knowledge and achievements on the reconstruction of reduced-area full-resolution images, originally encouraged by the radiation dose exposure reduction in medical imaging and where the Wavelet Transform (WT), along its different representations, proved to be an effective tool given its time-frequency localization capabilities [4], [5]. Such research has been commonly named as Wavelet-based local reconstruction, and has been reported to be useful in other application areas such as Nano and Micro Tomography [6], [7]; Terahertz Tomography [8], and Dental Radiology [9].

Of special interest is the 2D fast wavelet transform (2D FWT), employed in [5] and [10]. In addition to achieving local reconstruction, it allows projection data to be processed in a multi-resolution scheme. Such a feature proves to be of great benefit, when realizing its similarities with the parallel algorithm proposed in [11]. In that algorithm, a frequential decomposition of projection data is performed with the aim to back-project every component separately. The subsequent merger into a final image notably speeds up the image reconstruction process.

In this work we propose an algorithm combining the wavelet-based reconstruction of reduced image areas [5], [10]; and the parallel reconstruction from frequential sub-band decomposition of projection data [11]. The outline of the paper is as follows: Section II covers the background theory involved in the algorithm development; tomography image reconstruction, the wavelet transform and the multi-resolution representation. Section III details the implementation of the algorithm. The results are shown in section IV and the functionality of the approach is discussed in section V.

II. Background

A. Image Reconstruction from Projection Data.

In Tomography, as well as in other imaging techniques, the Radon Transform (RT) is the mathematical tool employed to map an unknown density distribution (object) $(x,)$ onto attenuation line integrals passing across it. In 2D, the analytical expression yielding the set of parallel line integrals is given by:

$$g(\theta,r) = \int_{-\infty}^{\infty}\int_{-\infty}^{\infty} f(x,y)\delta(x\,cos\theta + y\,sin\theta - r)dxdy, \quad (1)$$

where θ is the angle between the line normal and the x-axis, and r the distance from the rotation origin. Line integrals collected (e.g. by a detector array) at the same angle θ are grouped in a projection and the set of projections taken at all angles constitutes the sampled RT of the object. The 2D graphical representation of RT (the "sinogram") is given by a stack of all projections ordered by angle, each projection contributing with a row of pixel intensities determined by the values of the constituent line integrals.

An important property, utilized to solve the inverse problem of recovering $f(x,y)$ from projection data, is given by the Fourier Slice theorem, stating that the values calculated by the Fourier transform $G(\theta,\omega)$ of a projection at an angle θ:

$$\mathcal{F}_{1D}[g(\theta,r)] = G(\theta,\omega), \quad (2)$$

populate a "diagonal slice" at the same angle θ within the 2D Fourier image $F(u,v)$ of the object. Therefore, by taking the Fourier transform of the measured projection data at a

Manuscript received October 15, 2015.

Jorge Guevara Escobedo (jorge.guevaraescobedo@manchester.ac.uk) and Krikor B. Ozanyan (k.ozanyan@manchester.ac.uk) are with the School of Electrical and Electronic Engineering, The University of Manchester, M13 9PL, Manchester, UK. JGE wishes to acknowledge the financial support of Consejo Nacional de Ciencia y Tecnología (CONACyT), Mexico, for a doctoral studentship.

sufficient amount of angles to assemble a well sampled representation of the object's Fourier space, the solution to the inverse Radon problem is reduced to taking the 2D inverse Fourier transform

$$f(x,y) = \mathcal{F}_{2D}^{-1}[F(u,v)]. \quad (3)$$

In a practical implementation, it is not realistic to obtain projection data that fully covers the Fourier space. Therefore, the Filtered Back-projection (FBP) method is used to account for adjustment of the integration limits in the Fourier inversion, along with a change from Cartesian to polar coordinates. The FBP is mathematically defined by

$$f(x,y) = \int_0^{\pi} \int_{-\infty}^{\infty} G(\theta,\omega)|\omega| e^{j2\omega r}\, d\theta d\omega, \quad (4)$$

where $|\omega|$ is the Jacobian of the coordinate system transformation and acts as a ramp filter suppressing the low frequencies close to the origin. The above formula can be split into two steps: the filtering of projection data

$$Q(\theta,r) = \int_{-\infty}^{\infty} G(\theta,\omega)|\omega| e^{j2\omega r}\, d\omega, \quad (5)$$

and the back-projection

$$f(x,y) = \int_0^{\pi} Q_{\theta}(x\cos\theta + y\sin\theta) d\theta, \quad (6)$$

where $x\cos\theta + y\sin\theta = r$.

A more detailed explanation and the strict derivation of the FBP expression are available in [12].

B. Global character (non-locality) of the standard FBP

While the FBP attracts interest, due to its high computational efficiency [13], its functionality is limited by the availability of sufficient projection data, equi-spaced in θ and r [14]. In cases when access restrictions prevent the collection of complete data or measurements need to be limited only to a region of interest, (4) is not the most indicated reconstruction strategy. This is due to the non-locality of the standard FBP caused mainly by the ramp filter $|\omega|$, and particularly its discontinuity at the origin. The latter results in the spread of projection data support in the space domain.

This problem has been addressed under different names: i) Reconstruction from truncated projections [14], ii) Incomplete data problem [15], iii) Local Tomography [16], iv) The interior Radon Transform [17] and v) Tomography from scarce measurements [18]. All approaches serve the same purpose, to avoid the global dependency of the FBP and reconstruct an accurate image from compactly supported data.

Different approaches to local or limited data reconstruction have been reviewed in [19]–[21]. Work related to local Tomography has been generalized to different geometries [23], [24], as well as to emission [25], [26] and/or soft-field modalities [27].

Among different applications relevant to this work, the use of wavelet transforms emerges as one with the most promising methodology. This is due to the expectation that by employing a function having a sufficient amount of zero moments, the support will remain essentially unchanged. Wavelet filters are functions with compact support and can be constructed with a certain amount of zero moments [3], [28], [29].

C. The Wavelet Transform

The main idea behind the wavelet transform is to obtain information not only about the constituent frequencies of a signal, but also about the interval of time relevant to these frequencies.

As a cursory explanation, the continuous wavelet transform (CTW) is typically based on the complete temporal correlation between the input signal and dilated/expanded versions of a predefined finite length signal, derived from a mother wavelet. A match between a certain frequency in a temporal segment from the input signal and the wavelet being shifted along that segment is characterized by a high correlation coefficient and the contribution of that frequency, along with the temporal parameters of the segment, is flagged [30]. However, the CWT involves redundant processing of large data sets, not suitable for practical implementation.

A different representation scheme is the fast wavelet transform (FWT) proposed in [31], whereby a discrete signal is processed with a range of high/low pass digital filters and down-samplers; the result is a decomposition of the input signal into scale components differing in size by a factor of two, to its nearest higher scale.

Low and high pass filters, scaling functions (n) and wavelet function $\psi(n)$, respectively, are convolved with the input signal $x(n)$ to produce a pair of wavelet coefficients: approximations (lower frequencies) and details (higher frequencies). After filtering, the output wavelet coefficients' bandwidth is reduced by half, therefore by means of the Shannon theorem, these coefficients can be represented with as half as many of the samples contained in the original signal, without any loss:

$$W_s(k) = s(n) * x(n) \downarrow_{n=2k,k\geq 0}$$
$$W_{\psi}(k) = \psi(n) * x(n) \downarrow_{n=2k,k\geq 0}, \quad (7)$$

where * is the convolution symbol. To recover the original signal, the wavelet coefficients are up-sampled and reverse-filtered, resulting in two signals. The merger of these signals must be equivalent to the original signal, if the employed wavelet functions allow exact reconstruction. This is illustrated in Fig. 1.

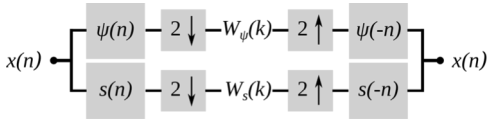

Fig. 1. FWT filter bank.

In a multi-scale representation, the approximation coefficients (k) become the input to a new frequency decomposition and the output coefficients will again contain only half as many samples as before.

For a 2D input signal, three wavelet functions are obtained from separable products between both scaling and wavelet

This article has been accepted for publication in a future issue of this journal, but has not been fully edited. Content may change prior to final publication. Citation information: DOI 10.1109/JSEN.2016.2546182, IEEE Sensors Journal

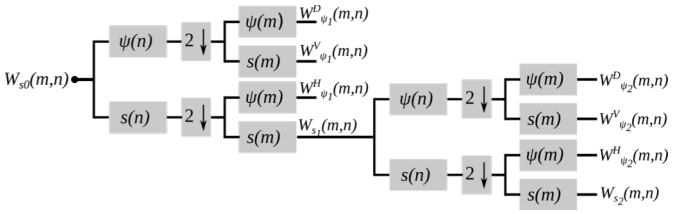

Fig. 2. Two-step 2D FWT.

functions. They quantify high frequency variations along different directions: horizontal, vertical and diagonal.

$$\begin{aligned} \Psi^H(m,n) &= s(m)\psi(n) && \text{Horizontal} \\ \psi^V(m,n) &= \psi(m)s(n) && \text{Vertical} \\ \psi^D(m,n) &= \psi(m)\psi(n) && \text{Diagonal} \end{aligned} \quad (8)$$

And the scaling function is as follows:

$$s(m,n) = s(m)s(n) \quad (9)$$

Performing the 2D FWT amounts then to the calculation of the 1D version along the rows and columns (m,n) of the 2D input signal.

$$\begin{aligned} W_\psi^H(m,n) &= \psi(m) * [x(m,n) * s(n) \downarrow_{n=2k}] \downarrow_{m=2k} \\ W_\psi^V(m,n) &= s(m) * [x(m,n) * \psi(n) \downarrow_{n=2k}] \downarrow_{m=2k} \\ W_\psi^D(m,n) &= \psi(m) * [x(m,n) * \psi(n)) \downarrow_{n=2k}] \downarrow_{m=2k} \\ W_s(m,n) &= s(m) * [x(m,n) * s(n)) \downarrow_{n=2k}] \downarrow_{m=2k} \end{aligned} \quad (10)$$

where $W_{\psi^H}(m,n)$, $W_{\psi^V}(m,n)$, and $W_{\psi^D}(m,n)$ are detail coefficients along horizontal, vertical and diagonal directions. $W_S(m,n)$ is the approximations coefficient, $x(m,n)$ is the input signal. Analogous to the 1D case, a multi-scale representation is achieved by the approximations wavelet coefficient becoming the input for a new wavelet transform iteration, as shown in Fig. 2. Thus, 4 coefficients are obtained at each scale: three separate detail coefficients and one approximations coefficient, corresponding to the lower scale component.

D. Wavelet-based Localized Tomography Reconstruction

1) Wavelet-modified ramp filtering

The main motivation in involving the wavelet transform in the FBP process is to avoid the support spread of projection data that occurs after the ramp filtering, since the latter emphasizes the global dependency of the measurements' overall support. As suggested in [3], for the accurate reconstruction of a ROI, the filtering stage of the standard FBP can be extended with the addition of essentially compactly supported functions, presenting a certain amount of zero moments. The low/high pass filters that act as wavelet/scaling functions in the 2D FWT, are functions of that type, and can be incorporated in (5) as follows.

$$W_{coeff}(x,y) = \int_0^{\pi}\int_{-\infty}^{\infty} G_\theta(\omega)[|\omega| W(\omega\, cos\theta, \omega\, sin\theta)] e^{j2\pi\omega s} d\omega d\theta \quad (11)$$

The above equation is the wavelet-based FBP, where $|\omega|(\omega cos\theta, \omega sin\theta)$ corresponds to the wavelet-modified ramp filter. W relates to the product between 1D high/low pass filters in Fourier domain and polar coordinates, being the last mentioned characteristic, necessary to match with the format of projection data. Separable products that correspond to each of the 2D FWT image coefficients are shown below:

$$\begin{aligned} W(\omega\, cos\theta, \omega\, sin\theta) = \\ S(\omega\, cos\theta, \omega\, sin\theta) = S(\omega\, cos\theta)\, S(\omega\, sin\theta) \\ \Psi^H(\omega\, cos\theta, \omega\, sin\theta) = S(\omega\, cos\theta)\, \Psi(\omega\, sin\theta) \\ \Psi^V(\omega\, cos\theta, \omega\, sin\theta) = \Psi(\omega\, cos\theta)\, S(\omega\, sin\theta) \\ \Psi^D(\omega\, cos\theta, \omega\, sin\theta) = \Psi(\omega\, cos\theta)\, \Psi(\omega\, sin\theta) \end{aligned} \quad (12)$$

It can be noticed from (12) that because of the Cartesian to polar re-gridding of low/high filter coefficients, the wavelet-modified ramp filters become angle dependent. Such dependency suffers the drawback that filter coefficients must be calculated for every projection angle separately. However, it also presents with the great advantage that the detail frequency components at a number of angles can be discarded because of their null effect in the projection data filtering. Unfortunately, this is not the case for the approximations frequency component, which incorporates all lower frequencies in all projection angles.

2) The back-projection operator and subsampling

It can be seen from (12) that unlike the standard FBP the filtering in the wavelet-based FBP generalization shifts the approach, from the frequency weighting of projection data within the Fourier space, to the decomposition into frequency components, as previously explained in section II *C*. This implies that back-projection has to be performed to create four different wavelet coefficient images, each of them half the size of the image yielded by the standard FBP. A remarkable consequence of such a characteristic is that the complexity involved in this operation is considerably reduced when implementing it parallel computation.

III. Proposed Parallel Multiscale Wavelet Reconstruction

A. Methodology

We adopt the approach proposed in [11], projection data is mapped onto a Fourier space divided into *B by B* adjacent squares with the objective to parallelize the reconstruction process. These squares define certain references to process

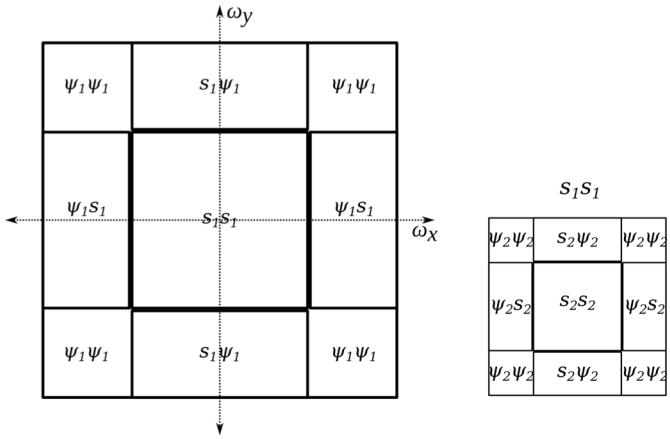

Fig. 3. Wavelet decomposition of the Fourier space. (a) One-step scale decomposition. (b) Two-step scale decomposition.

This article has been accepted for publication in a future issue of this journal, but has not been fully edited. Content may change prior to final publication. Citation information: DOI 10.1109/JSEN.2016.2546182, IEEE Sensors Journal

only projection data that concerns them. The result is a set of *B by B* frequency components which can be, independently and in parallel, back-projected onto less dense grids that are finally merged to form a single output image. By observing on Fig.3 how the 2D FWT tiles the Fourier space, it can be concluded that very similar properties are already implicit in the wavelet-based FBP. The main difference lies in the manner with which the combination of wavelet and scaling functions tiles the Fourier space into a fixed number of regions defining the frequencies that constitute each of the wavelet coefficients: three details and one approximations, as illustrated in Fig. 3(a).

If the approximations coefficient is used as the input of a new 2D FWT iteration, as shown in Fig. 3(b), the Fourier space can be tiled into more lower-scale regions, substituting the approximations coefficient by a set of new lower-scale wavelet coefficients. Although it is expected that a multi-scale decomposition contribute to the speed-up of the reconstruction process, the 2D FWT in its standard form, suffers from the requirement for the iterative computation of approximations at each scale.

This limitation can be bypassed through the use of the Noble identities [32], which allow the construction of an equivalent parallel multi-scale implementation of the 2D FWT in Fourier domain. The result is the substitution of the pyramidal configuration shown in Fig. 2, formed by low/high pass filters and downsamplers, into a scale-dependent set of filters and downsamplers. According to [10], for a non-pyramidal implementation, the low pass filter coefficients in the Fourier domain are as follows:

$$s_l(n) \leftrightarrow S_l(z) = \begin{cases} \prod_{q=0}^{l-1} H(2^q z) & l = 1,2,3\cdots \\ 1 & l = 0 \end{cases}, \quad (13)$$

and for high pass filters:

$$\psi_l(n) \leftrightarrow \Psi_l(z) = \begin{cases} \Psi(2^{l-1}z) S_{l-1}(z) & l = 1,2,3\cdots \\ 1 & l = 0 \end{cases}. \quad (14)$$

Fig. 4 shows the parallel implementation alternative to the 2D FWT. Apart from preserving the compact support and reducing the complexity of the back-projection operation, 2D FWT can be employed to obtain a multi-scale representation of the projection data, which if implemented in parallel, can speed up the reconstruction process dramatically.

B. Fast parallel algorithm

Under the concepts exposed in the previous sections, by exploiting the attributes provided by the 2D FWT when being employed in the image reconstruction process, we formulate a fast parallel algorithm. The main motivation in using the 2D FWT is to take advantage of its time-frequency localization properties and be able to reconstruct accurately, independently and in parallel, reduced area block components tiling together a full-size image. The main objective behind the reconstruction of block components is to reduce the overall reconstruction time, by considering only projection data corresponding to one block at a time.

A secondary feature, derived from the wavelet filtering of

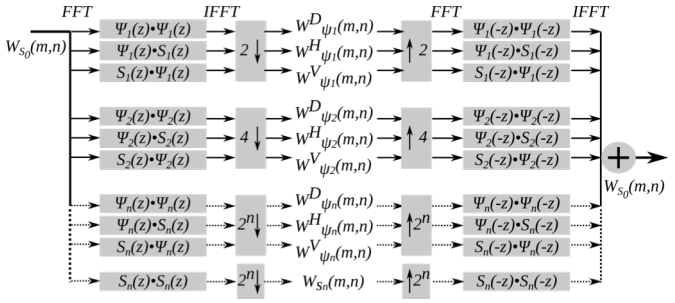

Fig. 4. Parallel 2D FWT.

projection data and the sampling theorem, allows back-projection of wavelet coefficient images to be performed without loss of information onto subsampled grids, half the size of the complete resolution image obtained through standard FBP reconstruction. This feature has an important implication in the speed-up of the reconstruction process; given the fact that back-projection is the most computationally expensive operation within the FBP [10].

Following the same line, by analyzing in Fig. 3 the breakdown of projection data within the Fourier space after wavelet filtering, it is obvious that certain projection angles have a null contribution (see Fig. 5) in the generation of detail coefficient images [12] and can be discarded without compromising the quality of the wavelet coefficient images. Conversely, when it comes to the generation of the approximations coefficient image, all projection angles must be considered (see top left example in Fig. 5(a)), therefore this advantage is only partially usable.

With the purpose to alleviate the consequences from such a restriction, the parallel multi-scale decomposition scheme was adopted in the development of this algorithm. As explained before, this scheme allows a frequential decomposition of projection data, in which approximations coefficient is only computed for the lower resolution component. This means that, in relationship with the sampling theorem, approximations coefficient can be backprojected onto the less dense grid, whose size is determined by the lower resolution component.

The algorithm presented in this work is a generalization of the FBP that has been designed by using MATLAB as software testing framework, having in mind a parallel implementation, either in hardware or in a software platform, capable of independently executing every component; e.g. in Simulink.

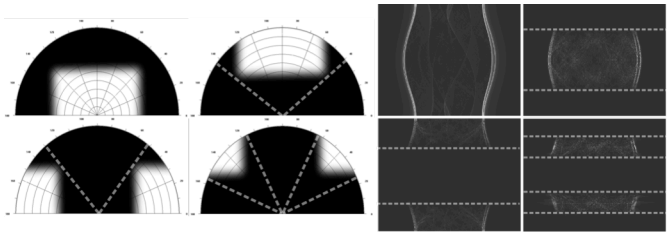

Fig. 5. Tomography projection data wavelet filtering. (a) 2D wavelet filters in Fourier domain and polar coordinates (0 to 180°), constructed by using the discrete Meyer FIR filter. (b) Wavelet-filtered projection data.

This article has been accepted for publication in a future issue of this journal, but has not been fully edited. Content may change prior to final publication. Citation information: DOI 10.1109/JSEN.2016.2546182, IEEE Sensors Journal

C. Computer Implementation of the standard FBP algorithm

In order to be able to adapt the standard FBP to the purposes of this work, it was implemented in MATLAB as a customized version of the '*iradon*' function, used as a reference benchmark. The ramp filter design uses a method reported in [33] and [34], aiming to suppress the dc shift and inter-period interference artifacts. This is achieved by calculating an impulse response approximation of the ramp filter and matching the sampling interval to the bandwidths of the filter and the projection data, which are also zero-padded before the FFT is applied. Filtering is performed in the Fourier domain, and with the objective of reducing the algorithm complexity, only "positive" frequencies are processed. The already filtered projection data is complemented with its complex conjugate, and inverse FFT is calculated. The back-projection operator, along with linear interpolation, is performed as designed in the '*iradon*' function.

D. Implementation of the multi-scale parallel block reconstruction algorithm

As previously mentioned, the algorithm was formulated for a parallel implementation. The latter depends on the isolation between certain elements, chosen among those that do not rely on values obtained during the execution of the algorithm and can be calculated a priori, and those that are totally dependent.

1) Off-execution algorithm elements

The computation of the off-execution elements starts from the decision of the scale depth into which the projection data will be decomposed. This information is relevant for the calculation of wavelet and scaling functions, as well as to determine the size of the wavelet coefficient images at each scale. In the algorithm, this information also determines the area of the blocks in which the full-size image will be decomposed, which is the area of the lower scale coefficient image, e.g. for a 256×256 pixel image, if decomposed into l = 3 scales, the lower scale image area is given by 256×2^{-3}, which corresponds to a 32×32 pixel image. This means that the full-scale 256×256 pixel image will be divided into four 32×32 pixel coefficient images (one approximations and three details) at scale l = 3, three 64×64 pixel detail images at scale l = 2, divided into four 32×32 blocks, and three 128×128 pixel detail images at scale l = 1 composed by sixteen 32×32 blocks. This is illustrated in Fig. 6.

By having information about the resolution depth and area size of each of the wavelet coefficients images, as well as of the constituent blocks, it is possible to calculate the filter coefficients (scaling/wavelet functions) by which the projection data will be decomposed. For this operation, (13) and (14) are employed in order to obtain the filter coefficients corresponding to each scale. These filter coefficients along with the designed ramp filter, are used to create the wavelet modified filters, directly employed in the analytical expression given by (11).

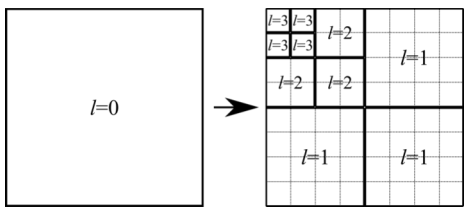

Fig. 6. Multiscale constituent block-breakdown

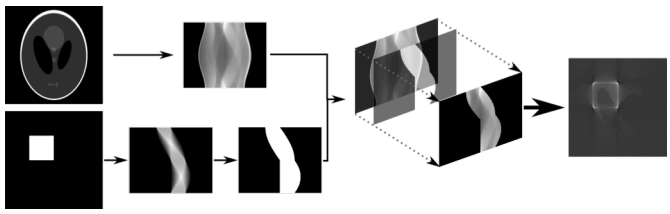

Fig. 7. Procedure of the projection data block-decomposition.

In order to decompose the projection data into several constituent blocks, a simple procedure was developed. It consists of generating synthetic phantoms representing the block area, within the field of view, that will be reconstructed individually. The RT from the block phantoms is then calculated and its support is obtained and converted to binary pixel values. The result is an array that is used as a template, to extract the projection data relevant for the reconstruction of the image block. This process is illustrated in Fig.7.

This approach has been developed with the purpose of avoiding the difficulties involved in the collection of off-centered data without degrading considerably the reconstructed image. In contrast to what is proposed in [3], this approach does not need extra padding of the projection data array, and therefore avoids the extra computational time involved when applying the filter.

2) On-execution algorithm elements

The on-execution elements are sequential portions of the algorithm that result as consequence of decomposing the reconstruction task into smaller ones. Each component task incorporates the computation that concerns only to the reconstruction of a wavelet coefficient block-tile image, at its corresponding scale, and is limited by its minimum data calculation dependency. Off-execution calculated variables are required in the execution of every block.

Each component task has the same base operators of the standard FBP: filtering of the projection data in the Fourier domain and its back-projection onto the real space grid. The difference lies in that every component task is dedicated to the reconstruction of a reduced area, at every scale, which is possible because of the 2D FWT incorporation. For the effect of dividing the full- size image reconstruction into a set of constituent block images, be reflected in speed gain, every component must deliver accurate images when provided only with data corresponding to the block area of interest.

Fig. 8 illustrates the processing carried out by each component task, when 3-level scale decomposition is desired. The first stage is the block decomposition of projection data, performed with the aid of support templates, for every scale except for the lower one, which determines the size and number of blocks in which the projection data is decomposed. FFT is then individually applied to the decomposed projection data and wavelet-based ramp-filtering is performed in the

This article has been accepted for publication in a future issue of this journal, but has not been fully edited. Content may change prior to final publication. Citation information: DOI 10.1109/JSEN.2016.2546182, IEEE Sensors Journal

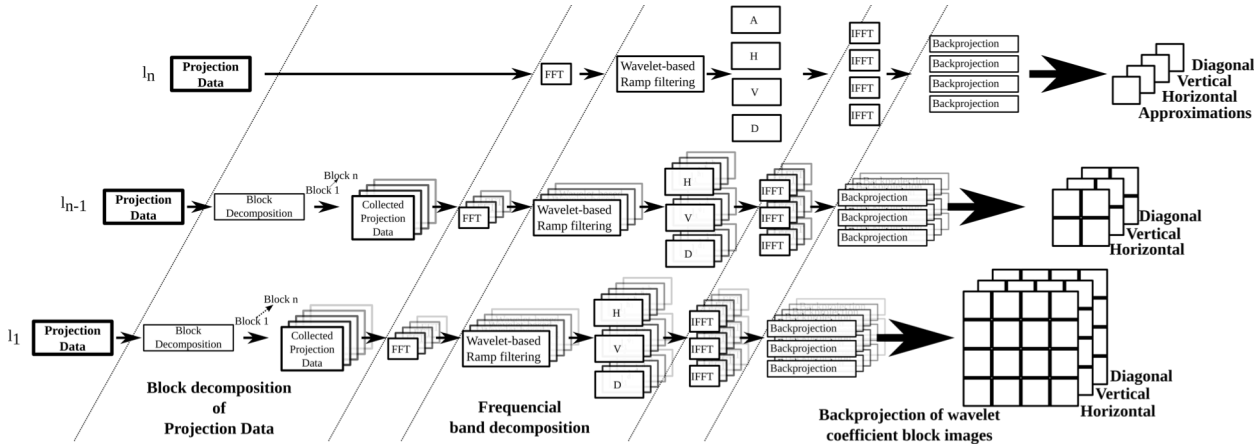

Fig. 8. Multi-scale parallel block reconstruction of wavelet coefficient images

Fourier domain, resulting in the frequential decomposition of every projection data component. Further, inverse FFT of the filtered projection data components is taken, followed by the back-projection onto subsampled grids to create wavelet coefficient block-images at each scale. Finally, wavelet coefficient images are obtained from the tiling of block-images. The full-size image at maximum resolution is obtained by the merger of all wavelet coefficient images through inverse 2D FWT in the space domain.

IV. Results

Results shown in this section were obtained with synthetic forward RT data generated by the MATLAB '*radon*' function, from 180 view angles equi-spaced within [0,180^o] by using the standard 512-pixel grid Shepp-Logan phantom. FBP image reconstruction was performed on a 512 by 512 pixel grid; no window function was employed in the filtering stage and linear interpolation was involved in back-projection operator. For frequential decomposition of projection data, a five-step multi-scale representation was obtained through the parallel 2D FWT. Wavelet coefficient images at each scale, except for scale l = 5, are divided into a set of 16×16 pixel constituent blocks; 4 for l = 4, 16 for l = 3, 64 for l = 2, and 256 for l = 1. The mother wavelet used for final results, was the symmetric and compactly supported "biorthogonal 2.4", which has a support length equal to five. The wavelet coefficient images, as well as the synthesized full-scale image, are shown in Fig.9.

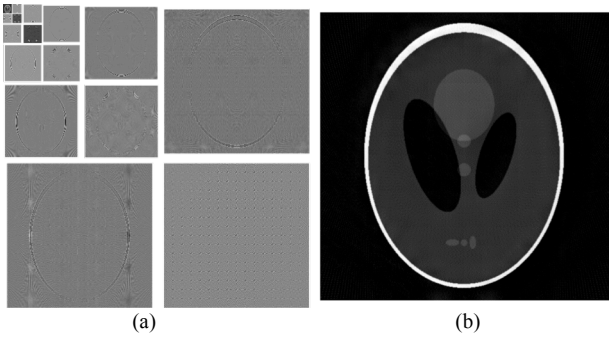

(a) (b)

Fig. 9. Reconstructed image from the wavelet-based multi-scale parallel block reconstruction algorithm. (a) Wavelet coefficients' images obtained at each scale; detail coefficient images for l=1,2,3,4,5 and approximations coefficient image for l=5. (b) Reconstructed output image at full scale l=0.

Fig. 10 shows the output of the three variants of the FBP algorithm: standard FBP, the 5-step multi-scale FBP and parallel-block multi-scale FBP. Table 1 shows quantitative error metrics to compare the images in Fig 10 (a) and (b), with the input phantom as the reference image. The adopted metrics are: average error (AVERR), normalized absolute error (NABS), and mean square error (MSE) [35]. For a metric more consistent with the human eye perception, the peak signal to noise ratio (PSNR) and the structural similarity index (SSIM) were also calculated [36]. The parallel block implementation, as such, does not result in additional errors.

With the objective to study the speed gain achieved in the parallel implementation compared to the standard FBP image reconstruction, time analysis of the algorithm execution was carried out. Measurements were taken by using the 'tic/toc' function in MATLAB 2012b, with a 3.1GHz Intel Quad Core i3 processor and 4GB RAM computer system, running a 64bit Linux Fedora 17 operating system. To ensure consistency, redundant measurements were taken by employing a single computer processor core.

In the first instance, time measurements were taken from the multi-scale wavelet-based FBP, with the objective of

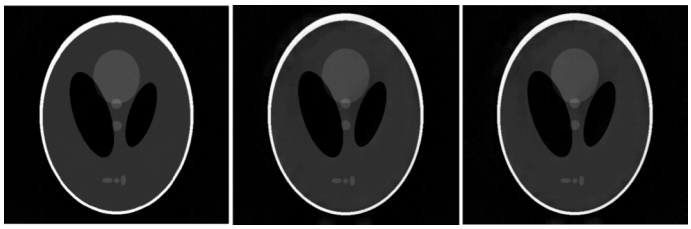

(a) (b) (c)

Fig. 10. Comparison between reconstructed images from different algorithms. (a) Standard FBP. (b) Wavelet-based multiscale five-step FBP. (c) Wavelet-based multi-scale five-step parallel block FBP.
Full-size images of Fig 10 (a) (b) and (c) are provided as separate media.

TABLE 1
QUANTITATIVE ERROR ANALYSIS

	AVERR	NABS	MSE	PSN	SSIM
Standard	0.0209	0.1691	0.0014	28.6426	0.6929
Multi-scale	0.0391	0.3168	0.0015	28.1788	0.4052

This article has been accepted for publication in a future issue of this journal, but has not been fully edited. Content may change prior to final publication. Citation information: DOI 10.1109/JSEN.2016.2546182, IEEE Sensors Journal

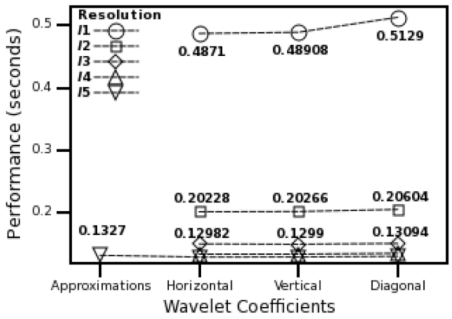

Fig. 11. Time performance of wavelet-based multi-scale five-step FBP.

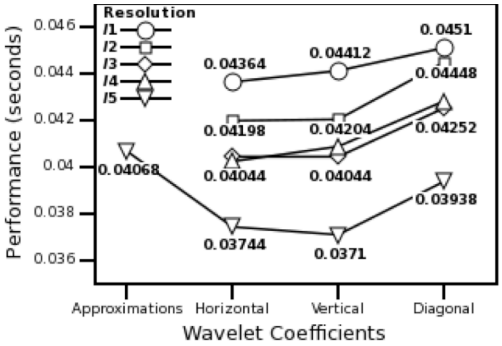

Fig. 12. Time performance of wavelet-based multi-scale five-step parallel block FBP.

showing the speed gain from the inclusion of the 2D FWT, without block decomposition. Fig. 11 shows the execution time, at each scale and for every wavelet coefficient image, calculated by the multi-scale wavelet-based FBP. The time performance shown includes upsampling and reverse-filtering. All execution times were considerably less than for the standard FBP, which under the same circumstances was measured to around be 1.7s.

For the parallel block decomposition algorithm, time performance was measured for each constituent block, for every wavelet coefficient, and at each scale. A detailed visual representation is impossible for this set of time performance measurements, as it would constitute a 512×512 pixel grid divided into 1024 16×16 pixel blocks. Therefore Fig. 12 presents the longest reconstruction time taken for a block within a specific scale and wavelet coefficient image. Again, upsampling and reverse-filtering are included. For the purpose of comparison, the longest time manifested in Fig. 12, 0.0451 s, is taken as the total time spent on the execution of the parallel algorithm. Fig. 13 shows the final time performance comparison between the three algorithms.

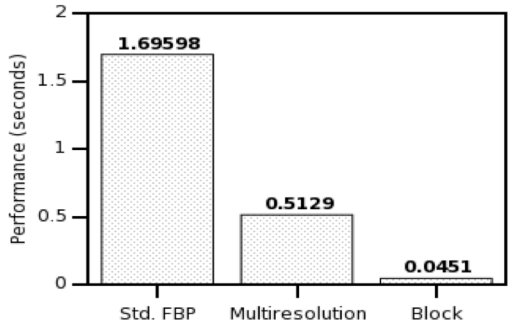

Fig. 13. Time performance between the three different reconstruction the algorithms; Standard FBP, the wavelet-based multi-scale five-step FBP and wavelet-based multi-scale five-step parallel block FBP.

V. Discussion

In this paper, an alternative algorithm to the widely used FBP has been presented. Due to its parallel implementation and block reconstruction approach, the image reconstruction speed is around 36 times faster than its standard counterpart. This speed performance gain is obtained at the expense of acceptable image degradation (see Fig. 10 and Table 1). It is interesting to note that while a two-fold error increase is calculated by AVERR and NABS, the metrics closer to human eye perception show a slight error reduction.

The work on the algorithm design demonstrated that the achievement of gain in speed at minimal image quality degradation strongly depended on the type of wavelet transform to be employed and the choice of the mother wavelet function.

The preferred choice of transform was the separable 2D FWT, mainly because it is amenable to a parallel implementation in addition to delivering a multi-scale representation. In the first instance, the importance of employing a wavelet filter that allowed an exact reconstruction scheme, while selecting the proper wavelet basis, was recognized. Attempts using different wavelet basis showed that, given the nature of the problem, a basis capable of preserving linear phase was required, which resulted in the choice of the symmetrical biorthogonal wavelets [37].

The choice in terms of wavelet filters was subject to a more complex process. This was driven mainly by a priori knowledge, derived from the understanding of the tomography problem, as well as from the test results during the algorithm design. An indicator of the localization in Fourier domain is regularity and is determined by the wavelet filter smoothness. Higher regularity allows more accurate frequential decomposition, but at the expense of higher amounts of filter coefficients, resulting again in speed loss.

After managing to achieve exact inversion of the 2D FWT, the major concern was to evaluate biorthogonal wavelet filters constructed with a different number of zero moments, supports and number of coefficients. The number of zero moments had a direct implication in the block-reconstruction accuracy, because it represents an indicator of the localization in space and is proportional to the support, which means that the higher the space localization, the less compact the support and the higher demand on computational resources. In the suggested algorithm, this was accounted for when deciding the amount of data to be collected for the reconstruction of constituent blocks: higher zero moments wavelets delivered higher quality reconstructed block images, at the expense of more data processing needed, resulting in less speed gain.

In conclusion, we have shown that tiled-block image

reconstruction by wavelet-based, parallel filtered back-projection leads to more than an order of magnitude gain in speed, compared to standard FBP, with acceptable image quality. This motivates future work in embedding such algorithms in programmable hardware, such as FPGAs.

REFERENCES

[1] J. Radon, "On the Determination of Functions from Their Integral Values along Certain Manifolds.," *IEEE Trans. Med. Imaging*, vol. 5, no. 4, pp. 170–176, 1986.

[2] G. N. Hounsfield, "Apparatus for examining a body by radiation such as x gamma radiation," *Pat. Prior. Date Prior. date 23 Aug 1968, United Kingdom Gt. Britain North. Irel.*, p. Medium: X; Size: Pages: 14, 1976.

[3] J. DeStefano, "Wavelet Localization of the Radon Transform," *IEEE Trans. Signal Process.*, vol. 42, no. 8, pp. 2055–2067, 1994.

[4] M. Holschneider, "Inverse Radon transforms through inverse wavelet transforms," *Inverse Probl.*, vol. 7, no. 6, pp. 853–861, 1991.

[5] F. Rashid-Farrokhi, K. J. R. Liu, C. A. Berenstein, and D. Walnut, "Wavelet-based multiresolution local tomography," *IEEE Trans. Image Process.*, vol. 6, no. 10, pp. 1412–1430, Jan. 1997.

[6] M. Costin, D. Lazaro-Ponthus, S. Legoupil, P. Duvauchelle, and V. Kaftandjian, "A 2D multiresolution image reconstruction method in X-ray computed tomography.," *J. Xray. Sci. Technol.*, vol. 19, no. 2, pp. 229–47, Jan. 2011.

[7] L. Li, H. Toda, T. Ohgaki, M. Kobayashi, T. Kobayashi, K. Uesugi, and Y. Suzuki, "Wavelet-based local region-of-interest reconstruction for synchrotron radiation x-ray microtomography," *J. Appl. Phys.*, vol. 102, no. 11, p. 114908, 2007.

[8] X. Yin, B. Ng, and J. Zeitler, "Local computed tomography using a THz quantum cascade laser," *Sensors Journal, …*, vol. 10, no. 11, pp. 1718–1731, 2010.

[9] K. Niinimäki, S. Siltanen, and V. Kolehmainen, "Bayesian multiresolution method for local tomography in dental x-ray imaging.," *Phys. Med. Biol.*, vol. 52, no. 22, pp. 6663–78, Feb. 2007.

[10] A. H. Delaney and Y. Bresler, "Multiresolution tomographic reconstruction using wavelets," *IEEE Trans. Image Process.*, vol. 4, no. 6, pp. 799–813, Jan. 1995.

[11] T. Rodet, L. Desbat, U. M. R. Cnrs, L. T. Cedex, P. Grangeat, and R. Martyrs, "Parallel algorithm based on a grequential decomposition for dynamic 3D computed Tomography," *Proc. Int. Parallel Distrib. Process. Symp.*, vol. 00, no. C, 2003.

[12] F. Natterer, "The Mathematics of Computerized Tomography," *Medical Physics*, vol. 29, no. 1. p. 107, 2002.

[13] K. J. Batenburg and L. Plantagie, "Fast approximation of algebraic reconstruction methods for tomography," *IEEE Trans. Image Process.*, vol. 21, no. 8, pp. 3648–3658, Aug. 2012.

[14] K. Ogawa, M. Nakajima, and S. Yuta, "A Reconstruction Algorithm from Truncated Projections.pdf," *Med. Imaging, IEEE …*, vol. MI, no. 1, pp. 34–40, 1984.

[15] A. K. Louis, "Incomplete Data Problems in X-Ray Computerized Tomography," *Numer. Math.*, vol. 262, pp. 251–262, 1984.

[16] A. Faridani, E. L. Ritman, and K. T. Smith, "Local Tomography," *SIAM J. Appl. Math.*, vol. 52, no. 2, p. 459, 1992.

[17] P. Maass, "The Interior Radon Transform," *SIAM J. Appl. Math.*, vol. 52, no. 3, pp. 710–724, 1992.

[18] K. B. Ozanyan, P. Wright, M. R. Stringer, and R. E. Miles, "Hard-field THz tomography," *IEEE Sens. J.*, vol. 11, no. 10, pp. 2507–2513, 2011.

[19] A. Bilgot, L. Desbat, and V. Perrier, "FBP and the interior problem in 2D tomography," *Nucl. Sci. Symp. …*, vol. 0, no. 2, pp. 4080–4085, 2011.

[20] G. Wang, H. Yu, and B. De Man, "An outlook on x-ray CT research and development.," *Med. Phys.*, vol. 35, no. 3, pp. 1051–1064, 2008.

[21] G. Wang and H. Yu, "Meaning of Interior Tomography," *Phys. Med. Biol.*, vol. 161, pp. 5764–5767, 2013.

[23] X.-C. Wang, B. Yan, L. Li, and G.-E. Hu, "Cone-beam local reconstruction based on a Radon inversion transformation," *Chinese Phys. B*, vol. 21, no. 11, p. 118702, 2012.

[24] Y. Xia, A. Maier, H. G. Hofmann, F. Dennerlein, K. Mueller, and J. Hornegger, "Reconstruction from truncated projections in cone-beam CT using an efficient 1D filtering," vol. 8668, p. 86681C, 2013.

[25] F. Ben Bouallegue, J. F. Crouzet, A. Dubois, I. Buvat, and D. Mariano-Goulart, "Least-squares dual characterization for ROI assessment in emission tomography.," *Phys Med Biol*, vol. 58, no. 12, pp. 4175–4194, 2013.

[26] F. B. Bouallegue, "A macroquantification approach for region-of-interest assessment in emission tomography," *J. Comput. Assist. Tomogr.*, vol. 37, no. 5, pp. 770–782, 2013.

[27] H. Kwon, A. L. McEwan, T. I. Oh, A. Farooq, E. J. Woo, and J. K. Seo, "A local region of interest imaging method for electrical impedance tomography with internal electrodes," *Comput. Math. Methods Med.*, vol. 2013, 2013.

[28] T. Olson, "Optimal time-frequency projections for localized tomography.," *Ann. Biomed. Eng.*, vol. 23, no. 5, pp. 622–36, 1995.

[29] C. A. Berenstein and D. F. Walnut, "Wavelets and local tomography," *Wavelets Med. Biol. (Aldroubi*, no. 1, pp. 231–262, 1996.

[30] I. Daubechies, *Ten lectures on wavelets - (C B M S - N S F Regional Conference Series in Applied Mathematics)*. 1992.

[31] S. G. Mallat, "A Theory for Multiresolution Signal Decomposition: The Wavelet Representation," *IEEE Trans. Pattern Anal. Mach. Intell.*, vol. 11, no. 7, pp. 674–693, 1989.

[32] F. Tay and J. P. Havlicek, "Frequency implementation of discrete wavelet," pp. 167–171, 2004.

[33] A. C. Kak, Author, M. Slaney, G. Wang, and Reviewer, *Principles of Computerized Tomographic Imaging*, vol. 29. 2002.

[34] A. C. Kak, "Computerized Tomography with X-Ray, Emission, and Ultrasound Sources," *Proc. IEEE*, vol. 67, no. 9, pp. 1245–1272, 1979.

[35] E. P. A. Constantino and K. B. Ozanyan, "Sinogram recovery for sparse angle tomography using a sinusoidal Hough transform," *Meas. Sci. Technol.*, vol. 19, no. 9, p. 94015, 2008.

[36] Z. Wang, A. C. Bovik, H. R. Sheikh, and E. P. Simoncelli, "Image quality assessment: From error visibility to structural similarity," *IEEE Trans. Image Process.*, vol. 13, no. 4, pp. 600–612, 2004.

[37] M. Antonini, M. Barlaud, P. Mathieu, and I. Daubechies, "Image coding using wavelet transform.," *IEEE Trans. Image Process.*, vol. 1, no. 2, pp. 205–20, Jan. 1992.

Jorge Guevara Escobedo obtained his BEng in Electronics and Telecommunication Engineering and MSc in Electronics from the Autonomous University of the State of Hidalgo. Hidalgo, Mexico (2006) and the National Institute of Astrophysics, Optics and Electronics, Puebla, Mexico (2007). He gained industrial experience as Design Engineer in Puebla, before receiving in 2011 a Doctoral Studentship award from Consejo Nacional de Ciencia y Tecnología (CONACyT), Mexico. He was Doctoral Candidate and Postgraduate Teaching Assistant at the University of Manchester, UK and was awarded a PhD degree in 2016. His main interests are signal processing for imaging sensors, embedded signal processing and imaging.

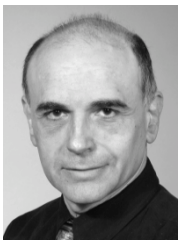

Krikor B. Ozanyan (M'95, SM'03) received his MSc degree in engineering physics (semiconductors) and PhD degree in solid-state physics, in 1980 and 1989 respectively. He has held previous academic and research posts in the University of Sofia, The Norwegian Institute of Technology (Trondheim, Norway), the University of Hull (UK), and the University of Sheffield (UK), working on projects ranging from Brewster-angle mid-IR spectroscopic ellipsometry and electron confinement in quantum wells and barriers, to the demonstration of the lasing at 333nm from strained MQW ZnCdS/ZnS structures and *in-situ* real-time optical monitoring of growth of III-V semiconductors in MBE and MOCVD reactors. His current interests are in the area of photonic sensors and indirect imaging (tomography) by optical modalities, signal processing for optical experiments, and spectroscopy with ultrafast laser sources. He is currently Head of Sensors, Imaging and Signal Processing at the University of Manchester and Visiting Professor at the University of Bergen, Norway.

Professor Ozanyan is Fellow of the Institute of Engineering and Technology, (UK, formerly IEE) and Fellow of the Institute of Physics (UK). He was Distinguished Lecturer of the IEEE Sensors Council in 2009-2010, Guest Editor of the IEEE Sensors Journal Special Issues "Sensors for Industrial Process Tomography" in 2005 and "THz Sensing: Materials, Devices and Systems" in 2012. He is currently Editor-in-Chief of the IEEE Sensors Journal.